Published in final edited form as:
J Phys Chem C Nanomater Interfaces. 2020 January 16; 124: 1317–1329. doi:10.1021/acs.jpcc.9b11039.

Photoelectrochemical Properties of SnO_2 Photoanodes Sensitized by Cationic Perylene-Di-Imide Aggregates for Aqueous HBr Splitting

Elisabetta Benazzi[a], **Karin Rettenmaier**[b], **Thomas Berger**[b,*], **Stefano Caramori**[a,*], **Serena Berardi**[a], **Roberto Argazzi**[a,c], **Maurizio Prato**[d,e,f], **Zois Syrgiannis**[d]

[a]Department of Chemical and Pharmaceutical Sciences of the University of Ferrara, Via Luigi Borsari 46, 44121 Ferrara

[b]Department of Chemistry and Physics of Materials, University of Salzburg, Jakob-Haringer-Straße 2a, A-5020 Salzburg, Austria

[c]ISOF-CNR, c/o Department of Chemical and Pharmaceutical Sciences of the University of Ferrara, Via Luigi Borsari 46, 44121 Ferrara

[d]Center of Excellence for Nanostructured Materials (CENMAT), INSTM UdR di Trieste, Department of Chemical and Pharmaceutical Sciences, University of Trieste, Piazzale Europa 1, 34127 Trieste, Italy

[e]Carbon Bionanotechnology Laboratory, CIC biomaGUNE, Paseo de Miramón 182, San Sebastian, Spain

[f]Basque Fdn Sci, Ikerbasque, Bilbao 48013, Spain

Abstract

Perylene-sensitized mesoporous SnO_2 films were used as electrodes for photoelectrochemical HBr splitting in aqueous solution. Upon AM 1.5 G illumination a 3-4 fold increase of the saturated photocurrent was observed when decreasing the pH of the aqueous solution from pH 3 to pH 0 (j^{max} = 0.05 ± 0.01 $mAcm^{-2}$ at pH 3 and 0.17 ± 0.02 $mAcm^{-2}$ at pH 0, respectively). A detailed spectroscopic and electrochemical analysis of the hybrid material was carried out in order to address the impact of interfacial energetics on charge separation dynamics. UV/Vis spectroelectrochemical measurements showed that the energy of semiconductor states in such systems can be adjusted independently from the molecular levels by varying proton concentration. Photoelectrochemical measurements and ns-µs transient absorption spectroscopy reveal that pH-related changes of the interfacial energetics have only a minor impact on the charge injection rate. An increase of the proton concentration improves charge collection mainly by retarding recombination, which in the case of Br^- oxidation is in critical competition with perylene regeneration. Control of the back recombination appears to be a key feature in heterogeneous molecular systems tasked to drive energetically demanding redox reactions.

*Thomas Berger: thomas.berger@sbg.ac.at; Stefano Caramori: cte@unife.it.

Europe PMC Funders Author Manuscripts

1 Introduction

The conversion of solar energy into chemical energy (solar fuels) has gained enormous interest in recent years [1–2]. Dye-sensitized photoelectrodes [3–4], *i.e.* wide band gap semiconductor films sensitized by suitable molecular dyes, were proposed as active materials in devices for water splitting [5] or water oxidation combined with CO_2 reduction [6–7]. Alternative methods for solar fuel generation are based on hydrohalic acid (HX) splitting. HX splitting involves the reduction of H^+ to H_2 and the concurrent oxidation of X^- to X_2. In particular, photoinduced HBr splitting represents an interesting approach since reaction products (H_2 and Br_2) can be used in redox flow batteries to generate electricity [8–10]. Most of the research work in this field concerns the design and the optimization of the photoanode since a molecular level approach towards water or HBr splitting requires a significant control over photophysical and electrochemical properties of the dye and the semiconductor material [11–12]. One of the major challenges is the development of visible light absorbing sensitizers, having sufficient driving force to carry out both electron injection into the semiconductor conduction band and hole (h^+) transfer to water oxidation catalysts, which are needed to lower the kinetic barrier for multi-electron transfer [13]. Even in the case of kinetically less demanding reactions, like bromide oxidation, strongly oxidizing ground states are required to produce Br_2 at a reasonable rate, thus storing > 1 eV/molecule. A huge series of metal complexes or organic molecules [14] was employed during recent years in conjunction with metal oxides [15–16]: recently, Meyer and co-workers reported an efficient Ruthenium polypyridyl photocatalyst for hydrobromic acid splitting [17] anchored on the surface of SnO_2/TiO_2 core−shell nanostructures with two phosphonic groups. Concurrently light-driven water splitting mediated by photogenerated bromine, which activated a water oxidation catalyst, was studied employing the same sensitizer [18].

Usually, the absorber is linked to the semiconductor surface via an anchoring group, such as the carboxylic acid group forming a mono- or bidentate configuration depending on surface composition and structure [19]. Alternatively, dye-semiconductor interactions based on π-stacking/hydrophobic forces were reported. In this context perylene units were employed as dyes [20–25] to carry out photooxidation reactions relevant to solar fuels generation. Following these examples, we have investigated charge injection and collection for semiconductor films sensitized by a cationic perylene based sensitizer ([(*N,N'-bis*(2-(trimethylammonium)ethylene)-perylene-3,4,9,10-tetracarboxylic acid *bis*-imide)]$(PF_6)_2$), herein abbreviated as PDI (Scheme 1) [24–26].

As previously reported [27], the most relevant advantage of dye-semiconductor systems based on hydrophobic interactions concerning performance stability, results from the adsorbate-substrate interaction, which does not suffer the hydrolytic cleavage of covalent links [28]. In this latter case, special surface treatment procedures are required to further stabilize the carboxylate or phosphonate bonds with the surface, typically consisting in atomic layer deposition of thin layers of inert metal oxides to protect the anchoring site and to hinder the access of the solvent. PDI is a visible absorbing molecule (energy gap *ca.* 2.5 eV) displaying a good thermal and photochemical stability and a ground state oxidation potential (E^0_{ox}) ~1.9 V *vs* normal hydrogen electrode (NHE), positive enough to drive most of the oxidation reactions having relevance in solar fuel formation processes [29–31]. On the contrary, the redox

potential of its excited state (E^{0}*) is scarcely reducing (-0.4 V *vs* NHE). Consequently only semiconductors with conduction band (CB) potentials E_{CB} more positive than -0.4 V vs NHE have the ability to quench oxidatively the PDI excited state. In the presence of aggregates, light absorption creates mobile excitons having $\pi-\pi^*$ character which separate at the interface with several metal oxides leading to electron injection into semiconductors like SnO_2 [26–27], Sb-doped SnO_2 (*i.e* ATO) [27] and WO_3 [26]. In particular, due to the rather high availability of tin, tin dioxide (SnO_2) is one of the most extensively studied transparent conducting materials. Typically prepared in the form of dense films, it exhibits the rutile (cassiterite) crystal structure in the space group $P4_2/mnm$, isostructural to TiO_2 and has a band gap of ~3.8 eV [32–33] which does not interfere with light absorption by the molecular sensitizer. The general principles of operation of the Dye Sensitized Photoelectrochemical Cell (DSPEC) for HBr splitting are reported in Scheme S1 of the Supporting Information (SI).

In general Dye Sensitized Solar Cells, conceptually similar to the photoelectrosynthetic cell object of the present investigation, have been shown to follow the diode equation according to [34]

$$J = J_L - J_0\left(\exp\left(-\frac{eV_j}{mkT}\right) - 1\right) \quad (1)$$

Where J_L is the limiting current density depending on the absorbed photon flux, $Vj = V + IR$ is the potential drop across the electrolyte/semiconductor junction, related to the applied bias V in the presence of the potential drop IR, where R can be regarded as the total series resistance of the cell. m is the ideality factor of the diode characterized by the equilibrium dark current density J_0. Both m and Jo are dependent on the specific chemical nature of the system. One can also view the photocurrent generation inside the solar device as a result of the flux of charge carriers along a given x direction by means of a combination of chemical and electrochemical potential gradient, according to

$$J = enu_nF + eD_n\frac{\partial n}{\partial x} \quad (2)$$

Where F is the electric field and u_n is the electron mobility, related to the diffusion coefficient D_n by

$$D_n = \frac{kT}{e}u_n \quad (3)$$

In the case of mesoporous semiconductors composed by a network of sintered nanocrystals[36] there is a significant population of localized states (L) in the band gap which are generally regarded as non-conductive, as opposed to conductive delocalized conduction band (CB) states. Charge transport thus occurs by trapping and detrapping of the carriers from and to the conductive states, and, if charge trapping and detrapping are sufficiently fast processes, transport can be described in terms of quasi-equilibrium charge densities in both localized and conductive states [35]. In this latter case the electron diffusion coefficient D_n can be expressed according to [37]

$$D_n = (1 + \frac{\partial n_L}{\partial n_{CB}})^{-1} D_0 \quad (4)$$

Where n_L and n_{CB} indicate the electron density in localized and conductive states respectively, and D_0 is the electron diffusion coefficient in the conductive states.

With TiO_2, charge transport is among the slowest processes occurring in Dye Sensitized Solar Cells, with a time constant of the order of 1 ms [38]. Nevertheless, with suitable redox couples, typically the I^-/I_3^- species, regeneration of the dye occurs on a time scale ca. 3 orders of magnitude shorter, preventing to a large extent electron recombination with the oxidized dye. The major charge recombination loss is thus related to the bielectronic reduction of I_3^-, a slow process (on the tens/hundreds ms time scale) at the photoanode, due to the poor electrocatalytic properties of both TiO_2 and FTO. This may result in nearly unit charge collection efficiency by sensitized TiO_2 thin films having a typical thickness ≤ 10 μm [39]. SnO_2 is characterized by higher electron mobility with respect to TiO_2 [40,41] but also by faster recombination channels, whereas, Br^- is thermodynamically more demanding (by ca. 0.5 eV) to oxidize compared to I^-. Thus, recombination of photoinjected electrons with the oxidized sensitizers could be a more considerable charge loss pathway with respect to the more studied TiO_2/I^- case [34]. On the other hand, in the DSPEC the oxidized form of the electron donor (Br_2 or Br_3^-) is either not initially present, or extremely diluted during the early functioning of the device, therefore the loss mechanism involving such species should be scarcely important during the initial stage of functioning of the device which we are considering in this work.

Thus, for the sake of characterizing the elementary charge separation events which control the energy conversion efficiency in the PDI-DSPEC based on SnO_2 we explore in the present work the impact of the electrolyte formulation on the surface energetics of the sensitized SnO_2 thin films by evaluating the effect of proton concentration on charge injection and recombination kinetics at the perylene/SnO_2 interface and on the related macroscopic photoelectrochemical electrode performance.

3 Results and Discussion

The deposition of non-sensitized SnO_2 particles from colloidal dispersion onto conductive fluorine-doped tin oxide (FTO) substrates, which is followed by a sintering step at 500 °C, results in uniform films consisting of particles with diameters of 60-70 nm, as previously confirmed by atomic force microscopy (AFM) [26]. The spontaneous adsorption of PDI onto the semiconductor surface results in the precipitation of both crystalline and amorphous PDI domains due to *pi*-stacking. The formation of the PDI aggregates is evidenced by the intensity reversal of the vibronic 0−0 and 0−1 bands in the absorption spectrum of a SnO_2-PDI film with respect to the PDI solution (Figure 1), paralleling a behaviour reported previously for PDI-sensitized Sb-doped SnO_2 (ATO-PDI)[27].

Current-voltage measurements recorded in the presence of 0.1 M Br^- as electron donor, are consistent with previous results [27], yielding a net photocurrent of *ca.* 0.1 $mAcm^{-2}$ (AM 1.5

G, 0.1 Wcm^{-2}, Figure 2a). The choice of bromide with respect to other halides is motivated by the following reasons:

- **i)** The lack of dark anodic processes on FTO (at least up to 1.2 V vs NHE) results in a wide and clear electrochemical window for evaluating electrode performance
- **ii)** The regeneration of the ground state of PDI^+ is thermodynamically strongly favourable (*i.e* -0.9 eV) [26]
- **iii)** Tri-bromide is an interesting species for energy storage and redox mediation[27]

Current-voltage curves (Figure 2a) were recorded at different proton concentrations, in order to investigate the repercussions of the pH on the performance of SnO_2-PDI electrodes. Explored electrolyte compositions were: 0.1 M NaBr / 1 M $HClO_4$ (pH 0); 0.1 M NaBr / 0.1 M $HClO_4$/ 0.9 M $NaClO_4$(pH 1) and 0.1 M NaBr / 10^{-3} M $HClO_4$ / 1 M $NaClO_4$ (pH 3). Acidic electrolytes were chosen to avoid interference from bromine oxo-anion formation. It is worth noting that not only the bromide concentration, but also the ionic strength, which is essentially determined by a large excess of ClO_4^- anions, was kept constant to avoid spurious effects related to variations in the electrolyte conductivity, which could influence the current-voltage characteristics. By operating at constant ionic strength we guaranteed that the aggregation state of PDI at the surface of the electrode was not changing significantly as a consequence of the surrounding electrolyte nature. Absorption spectra recorded on the photoanodes at different pH values (pH 0 – pH 3, Figure S1) show indeed practically overlapping absorption spectra at both pH 3 and pH 1. Only at pH 0 the absorption spectrum tends to become broader, with the intensity of the 0-0 and 0-1 vibronic band increasing with respect to the main band centred around 480 nm. The energy of the respective band maxima however remains unchanged, and such a small effect on the spectral shape at pH 0 could be due to some electrostatic perturbation between the positively charged semiconductor surface, and the positively charged PDI stack. The shape of the emission spectrum at pH 0 substantially overlaps with that recorded at pH 3 (Figure S2), and in both pH conditions the lifetime of the PDI excited state, probed at both 650 and 750 nm, yields very similar amplitude weighted values, on the order of 1.2-1.8 ns (Figures S3-S6). These values are related to the fraction of molecules decoupled from the semiconductor, whose excited states are not quenched by electron transfer. The slightly longer lifetime at pH 0 corroborates the indication of some perturbation of the stack which slightly reduces the rate of the nonradiative decay by internal conversion, but the general indication gained by these experiments is that the impact of electrolyte formulation on the intrinsic photophysical properties of PDI aggregates on the SnO_2 surface is quite modest. At pH 0 a SnO_2-PDI electrode yields the highest net photocurrent at 1.2 V (0.17 $mAcm^{-2}$), significantly exceeding the photocurrent detected at pH 1 (0.08 $mAcm^{-2}$) and pH 3 (*ca.* 0.05 $mAcm^{-2}$, Figure 2a). The photocurrent onset potential changes from 0.66 V at pH 0 to 0.60 V at pH 1 and *ca.* 0.50 V at pH 3 consistent with a Nernstian shift of 59 mV *per* pH unit. IPCE spectra are consistent with the PDI absorption profile on SnO_2, showing that the excited state of PDI is responsible for photocurrent generation. Furthermore, the IPCE is in good agreement with the trend observed under steady state photocurrent-voltage measurements, showing the best photo to current conversion efficiency (at 470 nm) of *ca.* 4% at pH 0 and a decrease in the

order pH 0 > pH 1 > pH 3 (Figure 2b). Figure S7 shows the photocurrent spectra, and their integral affording the integrated photocurrent, whose values are roughly in the ratio 1 (pH0) : 1/3 (pH1) : 1/4 (pH3), consistent with the limiting photocurrents reported in Figure 2.

IPCE can be expressed as the product of three efficiency terms, according to

$$IPCE = \varphi_{inj}\eta_{coll}LHE \quad (5)$$

Where φ_{inj} is the injection quantum yield, η_{coll} is the electron collection efficiency at the collector contact of the photoanode and LHE is the wavelength dependent Light Harvesting Efficiency. In the DSPEC, without Br_3^- initially present, under the relatively weak monochromatic illumination typical of quantum yield measurement combined to the anodic bias which sweeps charge at the maximum rate, we can consider that losses by electron recapture by the oxidized electron donor are negligible and that $\eta_{coll} = \frac{k_{reg}}{k_{rec} + k_{reg}}$ where k_{reg} and k_{rec} are the pseudo-first order rate constants for the regeneration of the PDI sensitizer by Br^- and for the recombination with electrons photoinjected into SnO_2.

One possible reason for the higher efficiency at pH 0 could be an increased driving force for charge injection from the PDI aggregates into the semiconductor, resulting from a positive shift of the Fermi level of the metal oxide, for which protons are potential-determining ions. In such a case, electron injection into the oxide would constitute the rate-determining step of the overall photoelectrochemical reaction. The rate constant related to the electron transfer (*i.e* electron injection) from PDI* to SnO_2, can be calculated according to Marcus equation[43]:

$$k_{et} = \nu_N \, ke^{\frac{-\Delta G^*}{RT}} \quad (6)$$

Where ν_N is the nuclear frequency factor, and k is the transmission coefficient, a parameter expressing the probability of the system to evolve from the reagent to the product configuration. The activation energy ΔG* can be expressed by

$$\Delta G^* = \frac{(\Delta G^o + \lambda)^2}{4\lambda} \quad (7)$$

where ΔG° is the free energy variation accompanying the process, while λ is the reorganization energy and represents the energy necessary to transform the nuclear configurations of the reactant and of the solvent to those of the products in a hypothetic isoergonic process. The driving force for the electron transfer from the PDI aggregates' excited state (PDI*) to SnO_2 (ΔG_{Et}) can be estimated by $\Delta G_{Et} = -e(|E^*_{ox} - E_{onset}|)$ as a function of pH. The onset potential (E_{onset}) of the cathodic capacitive current as determined from the negative going branch of a cyclic voltammogram (Figure S8b,c) is associated with the filling of band gap states close to the conduction band edge [44]. Rather than using the photoanodic onset of the J/V curves in Figure 2, which bears the contribution of kinetic overpotentials for photocurrent generation, we used dark cyclic voltammetry in inert

electrolytes to gain information on the energetic distribution of trap states in the mesoporous semiconductor film, [44–45] which may influence the dynamics of both injection and charge recombination. For non-sensitized SnO_2 electrodes at pH 1 the current onset was identified at E_{onset} ~ 0.4 V vs NHE [27] (Figure S8b). To investigate the impact of dye adsorption on the interfacial energetics cyclovoltammetric scans of PDI-sensitized SnO_2 electrodes were recorded. Upon PDI adsorption the onset potential shifts by ~ 5-10 mV towards more positive potentials (Figure S8b) due to changes of the oxide surface charge. Indeed such a shift is in perfect agreement with zeta potential measurements on aqueous dispersions of non-sensitized and PDI-sensitized SnO_2 particles (Figure S8a). The zeta potential of non-sensitized SnO_2 particles in pure water (pH 5) is –30 mV indicating an electrostatic stabilization of the suspension. At decreasing pH values the zeta potential shifts positive. The isoelectric point is observed at pH 3 – pH 4 in accordance with literature[42,46]. The functionalization of semiconductor particles with the dicationic dye, PDI, leads to a small zeta potential shift towards more positive values (by *ca.* 10 mV).

The cyclic voltammograms of PDI-sensitized SnO_2 electrodes (Figure 3a) feature an additional cathodic process with a threshold at -0.1 V vs NHE. This process is tentatively assigned to the reversible dye reduction and the onset potential approximatively corresponds to the oxidation potential of the PDI excited state (E^*_{ox}) (Figure 3a). This interpretation is confirmed by potential-dependent UV/Vis/NIR absorption spectra of a nanostructured SnO_2 electrode in aqueous electrolyte at pH 1 (Figure 3b). Using the spectrum of an electrode polarized at 1.4 V vs NHE as the reference, we observe significant spectral changes both in the UV and in the NIR upon the application of potentials E < 0.4 V (*i.e.* potentials more negative than the onset potential for charge accumulation, E_{onset}). In the NIR we observe a broad absorption background with a signal intensity that increases monotonically toward higher wavelength. Furthermore, this signal gains intensity by applying more negative potentials. In addition, we observe a signal loss in the UV range at 288 nm. Both optical changes result from an increase of the electron concentration in the nanostructured films. The broad signal in the Vis/NIR range can be attributed to the excitation of free electrons in the semiconductor (Drude absorption) [46–48]. The bleach at 288 nm results from the population of band gap states near the conduction band, giving rise to an apparent increase of the bandgap (Burstein shift) [49–50]. Both signals are fully reversible upon positive electrode polarization at E > 0.4 V vs NHE. Similar optical changes are observed for PDI-sensitized SnO_2 electrodes (Figure 3c). In addition to the signals observed for non-sensitized electrodes, the bleaching of the dye gives rise to a signal loss at ~470 nm by applying -0.1 V vs NHE, consistent with the faradaic process detected by cyclic voltammetry (Figure 3d) [51].

To confirm the assignment of the spectral signature appearing at -0.1 V vs NHE to dye reduction, spectroelectrochemical experiments on an electrochemically inert substrate (*i.e.* ZrO_2) were undertaken. In this case, reduction occurs by charge hopping from the FTO, being ZrO_2 an insulating material at the potentials of interest. Upon reduction of the PDI aggregates adsorbed on ZrO_2 a featureless bleaching band centred at *ca.* 480 nm, accompanied by the simultaneous increase of bands at 540 nm and 730 nm, is observed (Figure S9). It is worth noting that the vibronic structure is clearly lost, consistent with the

ground state absorption. This fingerprint agrees with the spectral variations observed on SnO_2 electrodes at potentials more negative than -0.1 V vs NHE.

The influence of the proton concentration on the interfacial properties of the non-sensitized and the PDI-sensitized semiconductor oxide was investigated by comparing CVs and potential-dependent optical absorption spectra at different pH values (pH 1 and pH 3). Upon an increase of the proton concentration the CVs shift to more positive potentials consistent with a Nernstian shift of 59 mV per pH unit (Figure S10a), while the shape of the CVs remains essentially unchanged. In perfect agreement with CV measurements, the bleach of the absorbance at ~280 nm (Figure S10b,c), related to electronic occupation of empty band gap states close to the conduction band, presents the same potential shift per pH unit. On the contrary, dye reduction takes place at the same potential at pH 1 and pH 3 (*i.e* -0.1 V vs NHE), revealing that the dye energetics are substantially unaffected by pH (Figure 4a). This is corroborated by potential-dependent UV/Vis spectra of a SnO_2-PDI electrode (Figure 4b,c), which highlight the pH-dependent shift of the onset-potential for electron accumulation in the semiconductor (as tracked by the bleach at 288 nm) and the invariance of the threshold-potential for dye reduction (as detected by the bleach at 470 nm).[52]

These results show that pH variation provides a means to tune the semiconductor energy levels independent from those of the sensitizer, allowing to optimize interfacial charge separation, at least in the case of poorly reducing excited states like those of aggregated PDI. The estimated driving force for the electron transfer from the PDI aggregates' excited state (PDI*) to SnO_2 (ΔG_{ET}) at pH 0, at pH 1 and at pH 3, respectively, accounts for -0.61 eV, -0.55 eV and -0.44 eV (Figure 5), taking into account that E_{onset} varies from 0.51 V at pH 0 to 0.45 V at pH 1 and 0.34 V at pH 3 (Figure 4 and Figure S11) and (E^*_{ox}) remains essentially unaffected (*i.e* -0.10 V vs NHE, Figure 4). It has to be mentioned that charge accumulation at $E < E_{onset}$ is associated with the population of band gap states. The conduction band edge will be located at more negative potentials experiencing however the same pH-dependent displacement. If the limiting photocurrent was mainly controlled by charge injection, a Gaussian shape should emerge according to the Marcus equation (Equation 6) when representing the photocurrent as a function of ΔG^0. A Gaussian function was used to fit the saturation photocurrent (as extracted from Figure 5) whereas a negligible current for zero driving force was assumed. However, the fitting yielded values for the reorganization energy of ~ 4.6 eV, which are physically unreasonable at least compared to known literature values for electron transfer involving PDI species in organic solvents. These studies report average values in the range 1.2-1.4 eV, depending on the chemical nature of the solvent and of the donor/acceptor pairs [53–54]. Consequently, the photocurrent dependence on pH cannot be explained uniquely by the increase in the injection driving force at lower pH which results from SnO_2 band shifts due to the augmented proton induced positive surface dipole.

To investigate in detail the pH-dependence of recombination phenomena, we recorded photocurrent-voltage curves using different types of light perturbation: (i) continuous light excitation (AM 1.5 G, I = 0.1 $mWcm^{-2}$), (ii) manually chopped illumination (AM 1.5 G, I = 0.1 $mWcm^{-2}$) and (iii) simultaneous excitation by a pulsed laser (λ = 532 nm, I = 0.06 $mJcm^{-2}pulse^{-1}$) and by a continuous white light bias (AM 1.5 G, I = 0.1 $mWcm^{-2}$). As

described above we observe upon pH variation a shift (resembling approximately a Nernstian behaviour) of the potential range featuring a linear variation of the photocurrent. This potential range extends approximately from 0.70 V to 0.85 V at pH 0, from 0.60 V to 0.75 V at pH 1 and from 0.50 V to 0.65 V at pH 3 (Figure 6). At more positive potentials photocurrent saturation is observed at all proton concentrations. However, at potentials more negative from the range of linear photocurrent-potential relation we observe a strongly diverging behaviour at different proton concentrations. Whereas no significant photocurrent is observed in this low-potential region at pH 0, the photocurrent extends far beyond the linear region at pH 3 fading away at ~0.35 V. Such a photocurrent tail is observed to a minor extent also at pH 1. The discrepancy in the photocurrent response in this low potential range is even more visible at manually chopped illumination. Photoanodic transients recorded upon light chopping at pH 3 (Figure 6c) feature significant photocurrent spikes followed by sharp cathodic spikes when the light is turned off. Virtually no spikes are observed in the low potential region at pH 0 (Figure 6a). Again an intermediate behaviour is observed at pH 1 (Figure 6b), where current spikes are present, but less pronounced than at pH 3.

In order to elucidate the impact of recombination on the dynamics regulating charge separation and collection efficiency, photocurrent transients were collected as a function of the applied potential (Figure 6d,e,f) by irradiating the samples with the 532 nm harmonic (0.06 $mJcm^{-2}pulse^{-1}$) of a nanosecond Nd:YAG laser. In addition, the sample was exposed to a continuous white light bias with an irradiance of ca. 0.06 Wcm^{-2}. Scheme S2 summarizes the principles of the experiment under simultaneous excitation where we initially consider open circuit conditions and the presence of the dye at the surface was omitted for clarity. Essentially, under continuous illumination, a steady state population of electrons in the semiconductor (occupying both localized and conduction band states) is created, while holes are confined within the surface adsorbed PDI stacks. When the laser pulse is absorbed by the photoanode, an extra population of photoinjected electrons is instantaneously (for the time scale of the experiment) generated in an environment which already reflects, through the partial population of CB and trap states, the presence of PDI^+ at the semiconductor/electrolyte interface and a local surface concentration of photogenerated Br_3^-, the steady state condition of the photoanode under normal operational conditions. By slowly scanning the voltage under simultaneous excitation, photocurrent transients will be collected on top of the continuous background current, whose magnitude provides qualitative information about the charge collection efficiency in the photoelectrode at any applied potential. Thus various charge separation regimes could be immediately revealed. Furthermore integration of these photocurrent transients under constant voltage and white light illumination, allows to access directly the time constants for the charge collection across the semiconductor/electrolyte junction. Clearly, perturbative techniques like IMPS or EIS are available to obtain recombination and transport rate constants in photoelectrochemical devices [55]. Nevertheless all these techniques require a validated model to extract the relevant figures, which at present we have not established for the specific case of PDI/SnO_2 yet. Equally important, these experiments are rather slow, a multivoltage EIS requiring tens of minutes/hours depending on the frequency domain of the processes of interest. During this time the chemistry of the system should not evolve nor change significantly. While this condition can be satisfied with either stable regenerative cells or photoelectrochemical water splitting (where water is

consumed), this is not intrinsically true for HBr splitting, where the electrolyte composition *has to change* due to Br_3^- accumulation and H^+ consumption as a consequence of hydrogen evolution.

SnO_2 is transparent to the 532 nm laser radiation, which is only intercepted by the PDI aggregates, giving rise to charge injection. The laser pulse, having a *ca.* 8 ns FWHM duration induces thus an instantaneous positive photocurrent rise, producing on average 1 photocurrent transient per mV, allowing to track precisely the shape of the current-voltage curve (Figure 6d,e,f). At pH 0 it can be seen that photocurrent transients start to be observed at least 300 mV more negative than the onset of the linear photocurrent-potential region in continuous light exposure experiments (corresponding to steady state photocurrents). While the onset potential differs, there is no significant change in the slope of the transient photocurrent increase and the photocurrent increase recorded upon continuous light exposure. A significant flattening of the slope of the transient photocurrent increase with respect to the steady state photocurrent is observed, however, at pH 1 and pH 3 (Figure 6d,e,f). Importantly, we evaluated both for continuous and for pulsed light excitation those potentials where the photocurrent attains ~50 % of its maximum value i.e. $E(0.5j^{max})$. The difference between these two values decreases from pH 0 to pH 1 and pH 3.

In the plateau region, at potentials more positive than 0.8 V vs NHE, the maximum transient amplitude decreases from *ca.* 0.3 $mAcm^{-2}$ at pH 0 to less than 0.2 $mAcm^{-2}$ in the case of pH 3 electrolyte, with pH 1 being the intermediate case, around 0.2 $mAcm^{-2}$. The relative transient amplitudes are in qualitative agreement with the steady state photocurrent density recorded under sun-simulated continuous illumination corroborating (even in the presence of short excitation pulses) superior photocurrent generation and collection at pH 0 irrespective of the applied potential (Figure 6d-f). Upon laser pulsed excitation large anodic photocurrent transients appear at intermediate (pre-continuous-photocurrent-onset) voltages between 0.4 and 0.7 V vs NHE. These transients are observed during the on-time of the duty cycle of the laser (data points above the continuous green line in Figures 6d-f). They appear well below the threshold of the steady state photocurrent, which is represented by data points collected during the off-time of the duty cycle i.e. upon sample exposure to the continuous white light bias only (data points below the continuous green line).

The pronounced photocurrent transients point to strong recombination in this potential range. Overall recombination may result from different contributions such as electron back-transfer to the oxidized dye or electron transfer to oxidation products. All possible processes will occur in parallel under reactive conditions making a disentangling impossible. However, by using different analytical methods (photoelectrochemistry as well as transient absorption spectroscopy) and by choosing different reaction conditions (absence / presence of a hole acceptor) we will be able in the following to highlight some important aspects of recombination at the interface of PDI-sensitized SnO_2 electrodes.

The photocurrent transients at pre-continuous-photocurrent-onset voltages are particularly pronounced at pH 0, where the largest magnitude (j ~ 0.4 $mAcm^{-2}$) is reached just before the onset of the steady state photocurrent. In this potential region data points collected during the off-time of the duty cycle highlight a shallow local minimum located between 0.60 and

0.65 V vs NHE. Such a cathodic feature is ostensibly due to reduction of adsorbed Br_3^-, which can be clearly observed in the cyclovoltammetric scans of SnO_2-PDI electrodes upon continuous light excitation (Figure S13). CVs show a significant reduction wave due to adsorbed Br_3^- at potentials consistent with the voltammetric response of the Br^-/Br_3^- couple (Figure S12). This wave progressively disappears upon subsequent scans in the dark (Figure S13) as no further Br^- is generated under these conditions whereas Br_3^- is reductively consumed and removed from the interface. Interestingly, the electrochemical response of the Br^-/Br_3^- process is partly affected by pH, quite significantly on FTO and more marginally on glassy carbon electrodes, becoming more reversible at pH 0, indicating thus that reduction of Br_3^- to Br^- is faster at low pH. Large photoanodic transients are thus originated by the formation of a local surface excess of Br^- at potentials negative of or coincident with the Br_3^- reductive wave. The in-situ generated Br^- intercepts efficiently the extra population of PDI^+ created by the laser pulse, resulting in a sudden rise of photoanodic current, which, however, cannot be sustained at these potentials, due to fast recombination with adsorbed Br_3^-. Only for potentials sufficiently positive to contrast redox mediated recombination, (i.e. E > 0.65 V vs NHE at pH 0) a steady state photoanodic response is observed. A similar short-circuiting with surface adsorbed redox couples was previously reported with entirely different types of sensitized electrodes and the aqueous I^-/I_3^- couple [62]. It is interesting to note that part of the redox mediated recombination is very fast, and could not be observed with the conventional method of shuttering the solar simulator. Indeed, even in the presence of laser pulsed excitation, both at pH 3 and at pH 1, the pre-onset photoanodic transients are practically cancelled by fast recombination (absence of transient photocurrents in the shaded regions in Figures 6e and f). This process may involve both free (conduction band) electrons and electrons filling shallow traps. In Figure 6 it can be clearly seen that such a fast recombination component is absent at pH 0. In addition, the slope of the photocurrent increase is steeper at pH 0 than at pH 1 and at pH 3 both when recording upon continuous excitation or upon pulsed excitation. Consequently, the difference between the potentials where the photocurrent upon continuous or, alternatively, pulsed light excitation attains ~50 % of its maximum value i.e. $E(0.5j^{max})$ decreases from pH 0 to pH 1 and pH 3. All these observations point to a more significant contribution of recombination at higher pH values.

Both steady state and pulsed experiments thus concur to the evidence of better electron collection at pH 0. At strong anodic potentials, i.e. E > 0.8 V vs NHE both the photoanodic transients and the steady state current are significantly larger than at pH 3 and 1. Finally the superior charge collection observed at pH 0 cannot be explained by a slower electron recapture by Br_3^- at the exposed FTO back contact of the photoanode, in consideration of the electrochemical response of the Br^-/Br_3^-, becoming more reversible at such pH (Figure S12).

Integration of the photocurrent transients obtained under limiting photocurrent conditions, i.e. at applied bias > 0.8 V offers interesting insights, which are particularly evident for the pH 0 and pH 3 cases (Figure 7), representing the conditions where the photoanode presents the largest difference in photoelectrochemical performance. In Figure 7 besides noting that at pH 0 it is possible to extract almost twice the charge generated by the laser pulse with respect to pH 3 it is also evident that the process of charge collection extends up to the 20 ms time scale and that it occurs according to at least two distinct kinetic components having

different amplitudes. At both pH 0 and pH 3 there is a fast (F) component, which rises with a time constant of the order of 7×10^{-4} s and was slightly faster at pH 0 (6.7×10^{-4}s) than at pH 3 (7.8×10^{-4} s) followed by a slower (S) component with a time constant in the order of 10^{-2} s (0.010 s at pH 0 compared to 0.012 s at pH 3). The most significant difference between the two cases is the relative amplitude of the F and S components amounting to an S/F ratio of 2.3 at pH 0 which is almost twice that observed at pH 3 (1.2). This result speaks in favour of a slower recombination in the case of the pH 0 electrolyte which allows the fraction of electrons trapped in localized states to partially escape recombination, detrap and being collected at longer times, explaining thus the larger amplitude of the slow collection component. Clearly, owing to instrumental limits to the sampling rate in fast chronoamperometry mode (10^{-4}s), all the other kinetics occurring at comparable or shorter time scales are missed by this technique.

To substantiate the assumption of a decreased contribution of recombination in the high-potential range at high proton concentrations the recovery of the oxidized state of the dye was monitored at 430 nm. Measurements were performed in the absence of Br^- electron donor in order to avoid interference from the PDI regeneration kinetics and Br_3^- recombination. Recombination tracked by transient absorption spectroscopy thus only involves electron back transfer to the oxidized dye. Following a nanosecond pulse a weak (less than 1 mΔOD) long lived transient absorption is observed, which is sensitive to the applied anodic bias (vs a Pt counter electrode at pH 0; Table 1, Figure 8). At 0.4 V, that is prior to the onset of the steady state curve, the decay of the photogenerated oxidized state due to recombination with injected electrons is > 80% complete within 40 μs, with less than 20% of the initial amplitude surviving beyond this time interval. A monoexponential decay fitted reasonably well most of the experimental traces, affording a lifetime of 9.4 μs. Following polarization at 1 V, the dye recovery due to recombination became considerably slower, and, with a first order life time of *ca.* 15 μs, resulted only ca. 50 % complete within 50 μs from the laser pulse. This trend is confirmed upon 1.5 V polarization, where the transient trace is less than 20 % recovered, with a lifetime close to 60 μs. The latter value is however only a crude estimate, given that most of the initial ΔA amplitude survives well beyond the time frame of the experiment. This is consistent with the presence of long-lived holes localized on the sensitizer aggregates (PDI^+), which promote the appearance of photoanodic current when the sacrificial agent is present. Thus, the increased PDI^+ lifetime is well explained by withdrawal of electrons injected into the mesoscopic film by the back contact, reducing the general electronic density of SnO_2. From Figure 8 we can rule out a major role of the anodic bias in tuning charge injection: although the injection rate constant is well below the time resolution of our nanosecond spectrometer, the fact that the initial amplitude of the transient, proportional to photogenerated PDI^+ concentration, remains substantially unchanged, suggests that the barrier for charge injection is unaffected by the applied potential as expected for mesoporous films. Also, the observation in SnO_2-PDI photoanodes of a time constant for charge injection on the time scale of the order of 100 fs at open circuit [27] is consistent with a small barrier for charge injection and supports our previous assumption that the injection rate is not the main limiting factor in photocurrent generation in SnO_2-PDI photoanodes. Clearly this holds true for the fraction of PDI which is actually electronically coupled with the semiconductor and able to separate their excitonic

state at the semiconductor surface. Previous experiments carried out with easy to oxidize sacrificial agents, where dye regeneration is not an issue [26], suggested that there is a large fraction of PDI species which are not in the condition to inject, being not well coupled with the semiconductor surface. Residual emission from the sensitized SnO_2 surface, discussed previously, is also an evidence of that.

Comparative recombination kinetics were examined by holding the voltage at 1 V and by using two different electrodes immersed in two different electrolytes, one at pH 0 (1 M $HClO_4$) and the other one at pH 3 (10^{-3} M $HClO_4$ / 1 M $NaClO_4$). The voltage equal to 1 V was chosen because it corresponds, in both cases, to the plateau region of the respective current-voltage curves recorded at the same pH in the presence of Br^- as electron donor, where the maximum rate of electron generation and collection by the photoanode occurs. In the case of the pH 3 electrolyte, the plateau is reached at E > 0.9 V, while at pH 0 the limiting current is found at E > 1 V (Figure 2a). From Figure 9, where the transient amplitude was normalized to 1, in order to allow for a clear comparison of the time evolution of the 430 nm traces, it can be observed that recombination involving PDI^+ is accelerated at pH 3, showing a fast recombination component with a lifetime of 1.6 μs, having an amplitude of *ca.* 50 % of the initial PDI^+ population. Such component is followed by a slower decay, with a lifetime of *ca.* 20 μs but globally, after 50 μs, only 1/3 of the initial amplitude has survived recombination. By contrast, $PDI^+/e^-(SnO_2)$ recombination at pH 0 lacks the fast recombination component with ca. ½ of PDI^+ being present on the SnO_2 surface after 50 μs from the laser excitation. TA measurements carried out in the ms-s time scale, i.e. on the same time scale of the charge collection experiments, are challenging due to the small S/N ratio of PDI^+. It was nevertheless possible to show at the limits of the sensitivity of our spectrometer (i.e. with transient amplitudes ≈10^{-4} ΔA) that even under open circuit condition the oxidized state of the dye persists in 1 M $HClO_4$, showing diagnostic absorption bands around 410-430 nm and a structured absorption in the 680-830 nm range (Figure S14). Under positive polarization this latter absorption feature increased in amplitude, more than doubling at 1.5 V vs NHE and surviving well beyond the 20 ms time scale (Figure S15) consistent with the expected behaviour of PDI^+ which experiences a slower recombination when electrons are drawn to the collector electrode by the electrochemical potential gradient. These results also confirm that recombination spans a time scale of several orders of magnitude, ranging from 10^{-7} to 10^{-1} s and that there is about 1/10 of the initial PDI^+ population which undergoes very slow recombination via electron traps. On the other hand similar experiments at pH 3 did not lead to traces with acceptable S/N, meaning that most of the dye underwent recombination on earlier time scales, confirming indirectly the evidence gained by the experiments in the ns-μs time scale. As an unfortunate coincidence, we note that the presence of the PDI^+ absorption band in the red/NIR region of the spectrum prevented the direct spectroscopic observation of the dynamics involving trapped electrons. Finally we could comparatively determine that, at least at pH0, regeneration of PDI^+ occurs within the ms time scale (Figure S16) in the presence of 0.1 M Br^-. While the acceleration of PDI recovery was evident, regeneration (k_{reg} = 8.1 10^2 s^{-1}) was still under partial kinetic competition with recombination, resulting in η_{coll} of the order of 50 % at its best. Using a maximum IPCE ≈4 % and LHE ≈70 % from Figure 2 and equation (5), we can thus estimate φ_{inj} of the order of 12%.

The reduced contribution of recombination to the saturation photocurrent (i.e. the photocurrents in the high-potential range) at high proton concentrations may have different origins.

A higher electron mobility inside the mesoporous thin film may result from a mechanism of ambipolar diffusion where charge transport is accompanied by diffusion of charge compensating ions permeating the film. Increased electron mobility caused by a higher concentration of very mobile cations will invariably result in better electron collection. Consequently, the decrease in charge density available for recombination prolongs the life of photooxidized dyes anchored at the semiconductor surface. Yanagida et al. showed, in mesoporous TiO_2 films, that the electron collection increased when replacing large organic cations like $DMHI^+$ and TBA^+ by small cations like Li^+. The ambipolar electron diffusion coefficients were the highest in the presence of small high charge density cations, like Li^+ and Mg^{2+} [54]. Protons are considered to be highly mobile species in water, undergoing transport via Grotthus or “structural” mechanism which is essentially activationless and occurs on the sub-ps time scale [56]. However, H^+ are also known to adsorb strongly on metal oxides possibly giving rise to long lived trap states which could represent a useful charge reservoir, provided that recombination is sufficiently slow compared to charge transport and collection [57]. This was actually observed in the case of at least a fraction of photogenerated PDI^+, which was able to survive on time scales longer than those of electron collection. Compared to the pH 3 case, the marginally faster collection at pH 0, coupled to the consistently larger slow charge collection component points indeed to a predominant role of reduced recombination over a significantly faster electron transport.

In addition, electron mobility may be influenced by a transient accumulation of electrons and charge compensating protons in the subsurface region of semiconductor oxide particles (hydrogen doping) [58–59, 61]. Such a charge-transfer reductive in situ doping was observed previously upon light exposure of mesoporous TiO_2 and WO_3 electrodes and results in a transient photocurrent enhancement which was attributed both to the increase of electron mobility and deactivation of recombination centres upon the concerted uptake of electrons and protons. Particle/electrolyte and particle/particle interfaces in mesoporous electrodes are regions of high defect density. The defects may act as recombination sites exerting a deleterious impact on the photocurrent. Using impedance spectroscopy, recombination sites in SnO_2-based chalcogenide-sensitized solar cells have been associated with a monoenergetic distribution of band gap traps at the SnO_2 surface [60]. Passivation of the SnO_2 surface with TiO_2 overlayers lead to the elimination of these surface traps and, importantly, to a significant slow-down of recombination [60]. On anatase and rutile TiO_2 photoelectrodes cyclic voltammetry was used to map the density of discrete electron traps in the band gap, which were assigned to structural disorder at the contact between neighbouring crystalline nanoparticles[63]. Under illumination, these trap states showed a deleterious effect on photocurrent, favouring electron recombination. However, it was shown in a combined electrochemical and quantum chemical study that the energetics of these traps can be modified via an electrochemical doping (i.e., incorporation of electron/proton pairs), leading to a large enhancement of photoelectrode performance[56]. Such a charge transfer reductive doping may take place even at open circuit conditions in acidic electrolytes and strongly depends on electrolyte composition and film morphology[53]. A similar modification of

surface or surface-near trap states may give rise to the beneficial effect of high proton concentrations on the photocurrent as observed in the present study.

4 Conclusions

In the present work, the interfacial properties of non-sensitized and PDI-sensitized SnO_2 films were characterized with regard to possible applications in photoelectrosynthetic cells for hydrohalic acid splitting. A significant dependence of the photoanode performance with respect to $[H^+]$ concentration was observed, with the highest photocurrents being generated at pH 0. In order to characterize this effect, UV/Vis spectroelectrochemical investigations of the PDI-sensitized SnO_2 revealed a distribution of available electron states in the semiconductor. The energy of these states was slightly influenced (by a ca. 5 mV positive shift) by the adsorption of the cationic PDI aggregates while they could be tuned in a Nernstian fashion independently from the molecular levels by varying proton concentration. Nevertheless, ns-μs transient absorption spectroscopy allowed to conclude that the Nernstian stabilization has only a minor influence in tuning the charge injection rate from PDI, consistent with previous ultrafast measurements. Increased proton concentration acts mostly by improving charge collection and retarding recombination, which, in the case of Br^- oxidation, is in critical competition with PDI regeneration. Thus, the concomitant observation of larger photocurrent and longer PDI^+ lifetime at pH 0 cannot be convincingly explained by increased electron mobility with respect to the pH3 electrolyte, as only a small improvement on the electron collection time constants was observed in the former case compared to the latter. Rather, high proton concentrations may entail an energetic modification of recombination centres at the surface or in surface-near regions thus slowing down recombination. This study highlights that the control of back recombination appears to be a key feature in heterogenized molecular systems tasked to drive energetically demanding redox reactions.

Supplementary Material

Refer to Web version on PubMed Central for supplementary material.

Acknowledgement

This research was partly funded by the ENI Donegani research institute (Unife). K.R. and T.B. acknowledge financial support from the Austrian Science Fund (FWF): P28211-N36. Part of this work was performed under the Maria de Maeztu Units of Excellence Program from the Spanish State Research Agency – Grant No. MDM-2017-0720.

References

1. Lewis NS, Nocera DG. Powering the planet: Chemical challenges in solar energy utilization. Proc Natl Acad Sci U S A. 2006; 103
2. Lewis NS. Research opportunities to advance solar energy utilization. Science. 2016; 351:1920.
3. Brennaman, LMKAlibabaei; Norris, MR; Kalanyan, B; Song, W; Losego, MD; Concepcion, JJ; Binstead, RA; Parsons, GN; Meyer, TJ. Solar water splitting in a molecular photoelectrochemical cell. Proc Natl Acad Sci U S A. 2013; 110

4. Gao Y, Ding X, Liu J, Wang L, Lu Z, Li L, Sun L. Visible light driven water splitting in a molecular device with unprecedentedly high photocurrent density. J Am Chem Soc. 2013; 135:4219. [PubMed: 23465192]
5. Tachibana Y, Vayssieres L, Durrant JR. Artificial photosynthesis for solar water-splitting. Nature Photon. 2012; 6:511.
6. Arai T, Sato S, Kajino T, Morikawa T. Solar CO_2 reduction using H_2O by a semiconductor/metal-complex hybrid photocatalyst: enhanced efficiency and demonstration of a wireless system using $SrTiO_3$ photoanodes. Energy Environ Sci. 2013; 6:1274.
7. Sahara G, Kumagai H, Maeda K, Kaeffer N, Artero V, Higashi M, Abe R, Ishitani O. Photoelectrochemical Reduction of CO_2 Coupled to Water Oxidation Using a Photocathode with a Ru(II)–Re(I) Complex Photocatalyst and a CoO_x/TaON Photoanode. J Am Chem Soc. 2016; 138
8. Mei B, Mul G, Seger B. Beyond Water Splitting: Efficiencies of Photo-Electrochemical Devices Producing Hydrogen and Valuable Oxidation Products. Adv Sustain Syst. 2017; 1
9. Livshits V, Ulus A, Peled E. High-power H_2/Br_2 fuel cell. Electrochem Commun. 2006; 8:1358.
10. Cho KT, Ridgway P, Weber AZ, Haussener S, Battaglia V, Srinivasan VJ. High Performance Hydrogen/Bromine Redox Flow Battery for Grid-Scale Energy Storage. J Electrochem Soc. 2012; 159
11. Vannucci AK, Alibabaei L, Losego MD, Concepcion JJ, Kalanyan B, Parsons G, Meyer TJ. Crossing the divide between homogeneous and heterogeneous catalysis in water oxidation. Proc Natl Acad Sci. 2013; 110
12. Gao Y, Zhang L, Ding X, Sun L. Artificial photosynthesis–functional devices for light driven water splitting with photoactive anodes based on molecular catalysts. Phys Chem Chem Phys. 2014; 20
13. Swierk JR, Mallouk TE. Design and development of photoanodes for water-splitting dye-sensitized photoelectrochemical cells. Chem Soc Rev. 2013; 42:2357. [PubMed: 23081721]
14. Yu Z, Li F, Sun L. Recent advances in dye-sensitized photoelectrochemical cells for solar hydrogen production based on molecular components. Energy Environ Sci. 2015; 8:760.
15. Khan SUM, Khan SU, Al-Shahry M, Ingler WB. Efficient photochemical water splitting by a chemically modified n-TiO_2 . Science. 2002; 297:2243. [PubMed: 12351783]
16. Cristino V, Caramori S, Argazzi R, Meda L, Marra GL, Bignozzi CA. Efficient Photoelectrochemical Water Splitting by Anodically Grown WO_3 Electrodes. Langmuir. 2011; 27:7276. [PubMed: 21542603]
17. Brady MD, Sampaio RN, Wang D, Meyer TJ, Meyer GJ. Dye-sensitized hydrobromic acid splitting for hydrogen solar fuel production. J Am Chem Soc. 2017; 139
18. Sheridan MV, Wang Y, Wang D, Troian-Gautier L, Dares CJ, Sherman BD, Meyer TJ, Meyer GJ. Light-Driven Water Splitting Mediated by Photogenerated Bromine. Angew Chem Int Ed. 2018; 130:3507.
19. Kollhoff F, Schneider J, Li G, Barkaoui S, Shen W, Berger T, Diwald O, Libuda J. Anchoring of carboxyl-functionalized porphyrins on MgO TiO_2, and Co_3O_4 nanoparticles. Phys Chem Chem Phys. 2018; 20
20. Mishra A, Fischer MK, Bäuerle P. Metal-free organic dyes for dye-sensitized solar cells: From structure: Property relationships to design rules. Angew Chem Int Ed. 2009; 48:2474.
21. Wang R, Li G, Zhang A, Wang W, Cui G, Zhao J, Shi Z, Tang B. Efficient energy-level modification of novel pyran-annulated perylene diimides for photocatalytic water splitting. Chem Commun. 2017; 53:6918.
22. Kirner JT, Finke RG. Sensitization of Nanocrystalline Metal Oxides with a Phosphonate-Functionalized Perylene Diimide for Photoelectrochemical Water Oxidation with a CoO_x Catalyst. ACS Appl Mater Interfaces. 2017; 9
23. Kamire RJ, Materna KL, Hoffeditz WL, Phelan T, Thomsen JM, Farha OK, Hupp JT, Brudvig GW, Wasielewski MR. Photodriven Oxidation of Surface-Bound Iridium-Based Molecular Water-Oxidation Catalysts on Perylene-3,4-dicarboximide-Sensitized TiO_2 Electrodes Protected by an Al_2O_3 Layer. J Phys Chem C. 2017; 121:3752.
24. Wu LZ, Ye C, Li J-X, Wu H-L, Li X-B, Chen B, Tung C-H, Wu L-Z. Enhanced Charge Separation Efficiency Accelerates Hydrogen Evolution from Water of Carbon Nitride and 3,4,9,10-Perylene-

tetracarboxylic Dianhydride Composite Photocatalyst. ACS Appl Mater Interfaces. 2018; 10:3515. [PubMed: 29327911]

25. Bonchio M, Syrgiannis Z, Burian M, Marino N, Pizzolato E, Dirian K, Rigodanza F, Volpato GA, La Ganga G, Demitri N, Berardi S, et al. Hierarchical organization of perylene bisimides and polyoxometalates for photo-assisted water oxidation. Nature Chem. 2019; 11:146. [PubMed: 30510216]
26. Ronconi F, Syrgiannis Z, Bonasera A, Prato M, Argazzi R, Caramori S, Cristino V, Bignozzi CA. Modification of Nanocrystalline WO_3 with a Dicationic Perylene Bisimide: Applications to Molecular Level Solar Water Splitting. J Am Chem Soc. 2015; 137:4630. [PubMed: 25837588]
27. Berardi S, Cristino V, Canton M, Boaretto R, Argazzi R, Benazzi E, Ganzer L, Varillas RB, Cerullo G, Syrgiannis Z, Rigodanza F, et al. Perylene Diimide Aggregates on Sb-Doped SnO_2: Charge Transfer Dynamics Relevant to Solar Fuel Generation. J Phys Chem C. 2017; 121
28. Hanson K, Brennaman MK, Luo H, Glasson CR, Concepcion JJ, Song W, Meyer TJ. Photostability of Phosphonate-Derivatized, Ru^{II}Polypyridyl Complexes on Metal Oxide Surfaces. ACS Appl Mater Interfaces. 2012; 4:1462. [PubMed: 22316053]
29. Li C, Wonneberger H. Perylene imides for organic photovoltaics: yesterday, today, and tomorrow. Adv Mater. 2012; 24:613. [PubMed: 22228467]
30. Würthner F, Saha-Möller CR, Fimmel B, Ogi S. Perylene bisimide dye assemblies as archetype functional supramolecular materials. Chem Rev. 2016; 116:962. [PubMed: 26270260]
31. Kirner JT, Stracke J, Gregg BA, Finke RG. Visible-Light-Assisted Photoelectrochemical Water Oxidation by Thin Films of a Phosphonate-Functionalized Perylene Diimide Plus CoO_x Cocatalyst. ACS Appl Mater Interfaces. 2014; 6
32. Batzill M, Diebold U. The surface and materials science of tin oxide. Progr Surf Sci. 2005; 79:47.
33. Abello L, Bochu B, Gaskov A, Koudryavtseva S, Lucazeau G, Roumyantseva M. Structural Characterization of Nanocrystalline SnO_2 by X-Ray and Raman Spectroscopy. J Solid State Chem. 1998; 135:78.
34. Green ANM, Palomares E, Haque SA, Kroon JM, Durrant JR. Charge Transport versus Recombination in Dye-Sensitized Solar Cells Employing Nanocrystalline TiO_2 and SnO_2 Films. J Phys Chem B. 2005; 109
35. Bisquert J, Vikhrenko VS. Interpretation of the Time Constants Measured by Kinetic Techniques in Nanostructured Semiconductor Electrodes and Dye-Sensitized Solar Cells. J Phys Chem B. 2004; 108:2313.
36. Rettenmaier K, Zickler GA, Redhammer GJ, Anta JA, Berger T. ACS Appl. Mater. Interfaces. 2019; 11
37. Bisquert, J, Fabregat Santiago, F. Impedance spectroscopy: a general introduction and application to dye-sensitized solar cells. Kalyanasundaram, K, editor. CRC Press; 2010.
38. Peter LM, Duffy NW, Wang RL, Wijayantha KGU. Transport and interfacial transfer of electrons in dye-sensitized nanocrystalline solar cells. J. Electroanal. Chem. 2002; 524:127.
39. Hagfeldt A, Boschloo G, Sun L, Kloo L, Pettersson H. Dye-sensitized solar cells. Chem. Rev. 2010; 110:6595. [PubMed: 20831177]
40. Jousse D, Constantino C, Chambouleyron I. Highly conductive and transparent amorphous tin oxide. J Appl Phys. 1983; 54:431.
41. Shanthi E, Dutta V, Banerjee A, Chopra KL. Electrical and optical properties of undoped and antimony - doped tin oxide films. J Appl Phys. 1980; 51:6243.
42. Li N, Meng Q, Zhang N. Dispersion stabilization of antimony-doped tin oxide (ATO) nanoparticles used for energy-efficient glass coating. Particuology. 2014; 17:49.
43. Faulkner LR, Leddy J, Zoski CJ, Bard AJ. Electrochemical methods: fundamentals and applications. 1980
44. Bisquert J, Fabregat-Santiago F, Mora-Seró I, Garcia-Belmonte G, Barea EM, Palomares E. A review of recent results on electrochemical determination of the density of electronic states of nanostructured metal-oxide semiconductors and organic hole conductors. Inorganica Chimica Acta. 2008; 361:684.

Europe PMC Funders Author Manuscripts

45. Berger T, Monllor-Satoca D, Jankulovska M, Lana-Villarreal T, Gómez R. The electrochemistry of nanostructured titanium dioxide electrodes. Chem Phys Chem. 2012; 13:2824. [PubMed: 22753152]
46. Rodrigez-Santiago V, Fedkin MV, Wesolowski DJ, Rosenqvis J, Levov NS. Electrophoretic Study of the SnO_2/Aqueous Solution Interface up to 260 °C. Langmuir. 2009; 25:8101. [PubMed: 19594185]
47. Pankove, JI. Optical Processes in Semiconductors. Dover; New York: 1975.
48. Basu, PK. Theory of Optical Processes in Semiconductors. Oxford University Press; New York: 1997.
49. O'Regan B, Grätzel M, Fitzmaurice D. Optical electrochemistry I: steady-state spectroscopy of conduction-band electrons in a metal oxide semiconductor electrode. Chem Phys Lett. 1991; 183:89.
50. Cao F, Oskam G, Searson PC, Stipkala JM, Heimer TA, Farzad F, Meyer GJ. Electrical and optical properties of porous nanocrystalline TiO_2 films. J. Phys. Chem. 1995; 99
51. Kircher T, Löhmannsröben H-G. Photoinduced charge recombination reactions of a perylene dye in acetonitrile. Phys Chem Chem Phys. 1999; 1:3987.
52. Measurements at pH 0 have been omitted in these experiments due to the limited stability of the FTO substrate upon cathodic polarization for extended times.
53. Neuteboom EEE, Beckers EHA, Meskers SCJ, Meijer EW, Janssen RAJ. Singlet-energy transfer in quadruple hydrogen-bonded oligo(p-phenylenevinylene)perylene-diimide dyads. Org Biomol Chem. 2003; 1:198. [PubMed: 12929411]
54. Kambe S, Nakade S, Kitamura T, Wada Y, Yanagida S. Influence of the Electrolytes on Electron Transport in Mesoporous TiO_2-Electrolyte Systems. J Phys Chem B. 2002; 106:2967.
55. Bertoluzzi L, Ma S. On the methods of calculation of the charge collection efficiency of dye sensitized solar cells. Phys Chem Chem Phys. 2013; 15:4283. [PubMed: 23416949]
56. Woutersen S, Bakker HJ. Ultrafast vibrational and structural dynamics of the proton in liquid water. Phys Rev Lett. 2006; 138305:1.
57. Halverson AF, Zhu K, Erslev PT, Kim JY, Neale NR, Frank AJ. Perturbation of the Electron Transport Mechanism by Proton Intercalation in Nanoporous TiO_2 Films. Nano Lett. 2012; 12:2112. [PubMed: 22428871]
58. Idígoras J, Anta JA, Berger T. Charge-Transfer Reductive in Situ Doping of Mesoporous TiO_2 Photoelectrodes: Impact of Electrolyte Composition and Film Morphology. J Phys Chem C. 2016; 120
59. Márquez A, Rodríguez-Pérez MJ, Anta JA, Rodríguez-Gattorno G, Bourret GR, Oskam G, Berger T. Defects in Porous Networks of WO_3 Particle Aggregates. Chem Electro Chem. 2016; 3:658.
60. Huang Q, Li F, Gong YJL, Yang S, Yang L, Li D, Bai X, Meng Q. Recombination in SnO_2-Based Quantum Dots Sensitized Solar Cells: The Role of Surface States. J Phys Chem C. 2013; 117
61. Jimenez JM, Bourret GR, Berger T, McKenna PK. Modification of Charge Trapping at Particle/Particle Interfaces by Electrochemical Hydrogen Doping of Nanocrystalline TiO_2 . J Am Chem Soc. 2016; 138:491–5956. [PubMed: 26741640]
62. Caramori S, Cristino V, Argazzi R, Meda L, Bignozzi CA. Photoelectrochemical Behavior of Sensitized TiO_2 Photoanodes in an Aqueous Environment: Application to Hydrogen Production. Inorg Chem. 2010; 49:3320. [PubMed: 20210301]
63. Jankulovska M, Berger T, Wong SS, Gómez R, Lana-Villarreal T. Trap States in TiO_2 Films Made of Nanowires, Nanotubes or Nanoparticles: An Electrochemical Study. Chem Phys Chem. 2012; 13:3008. [PubMed: 22740436]

Europe PMC Funders Author Manuscripts

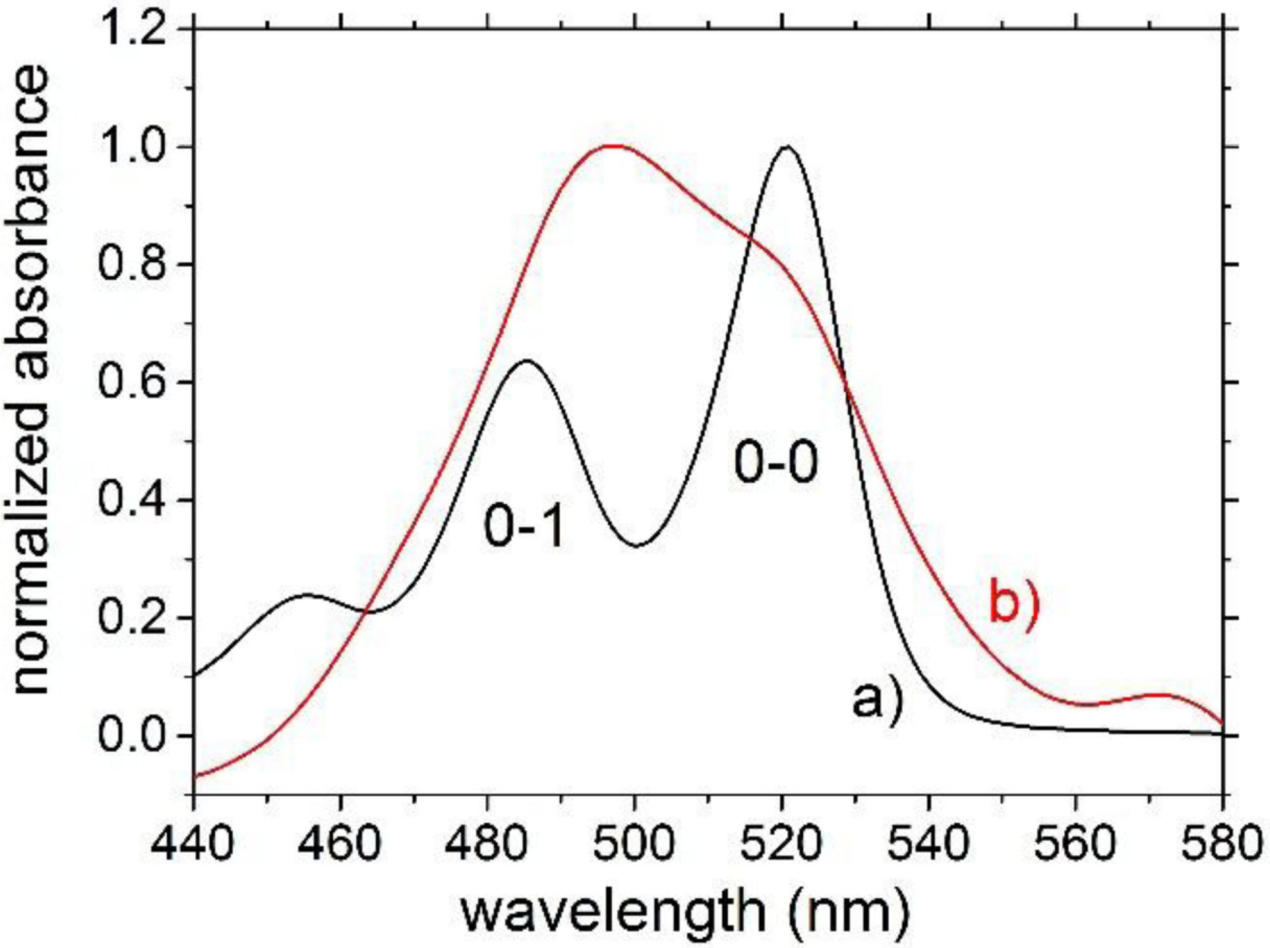

Figure 1.
Normalized absorption spectra of a) PDI dissolved in acetonitrile and b) a PDI-sensitized SnO_2 film.

Europe PMC Funders Author Manuscripts

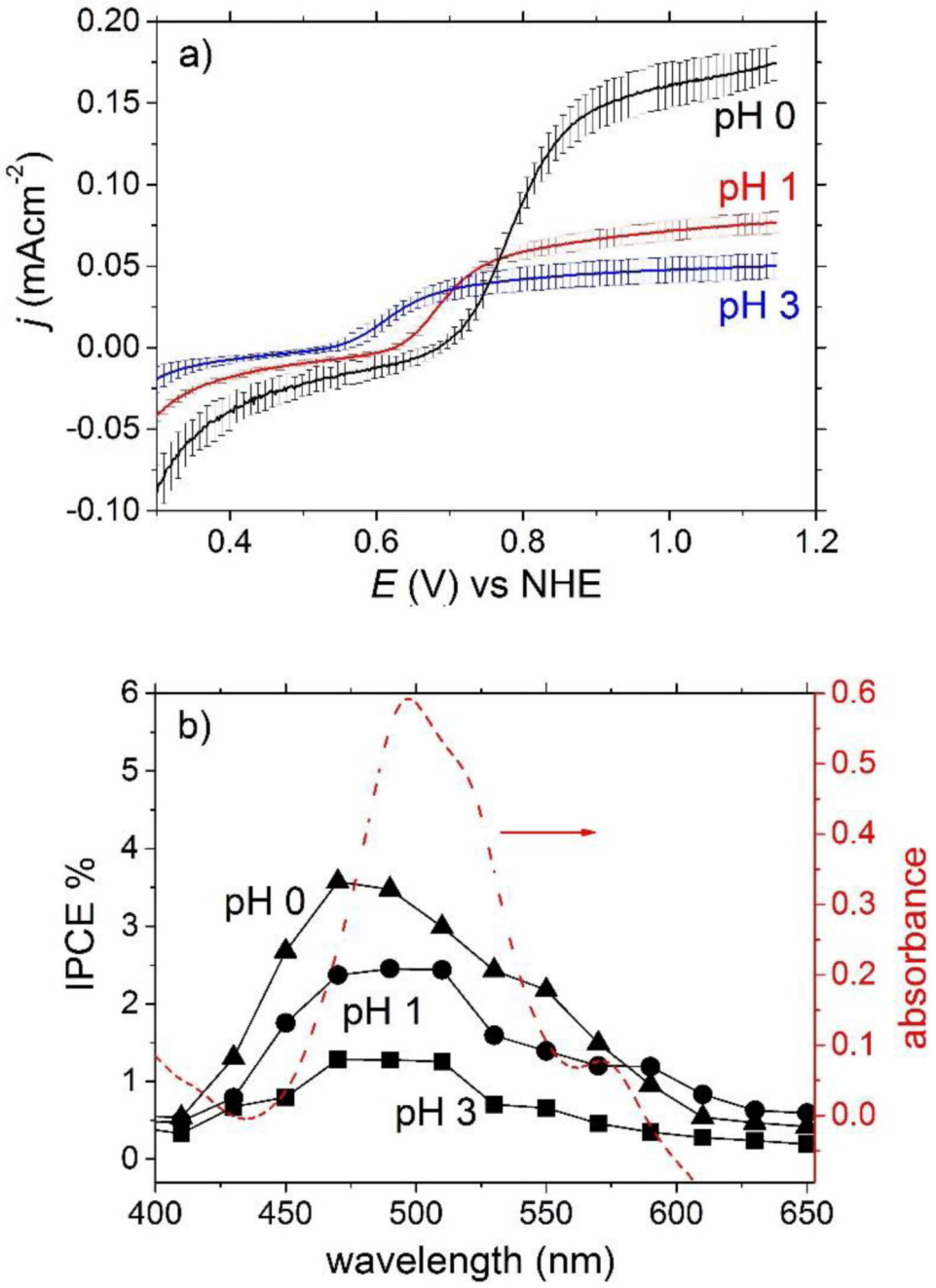

Figure 2.

a) Averaged steady-state current-voltage curves of SnO_2-PDI electrodes upon light exposure in aqueous electrolytes. b) IPCE curves recorded at constant 0.94 V vs NHE for a SnO_2-PDI electrode at different pH values. The dashed line represents the absorption spectrum of a SnO_2-PDI film. Electrolyte: 0.1 M NaBr / 1 M $HClO_4$ (pH 0); 0.1 M NaBr / 0.1 M $HClO_4$/ 0.9 M $NaClO_4$ (pH 1) and 0.1 M NaBr / 10^{-3} M $HClO_4$/ 1 M $NaClO_4$ (pH 3). Solar simulator: AM 1.5 G, I = 0.1 Wcm^{-2}.

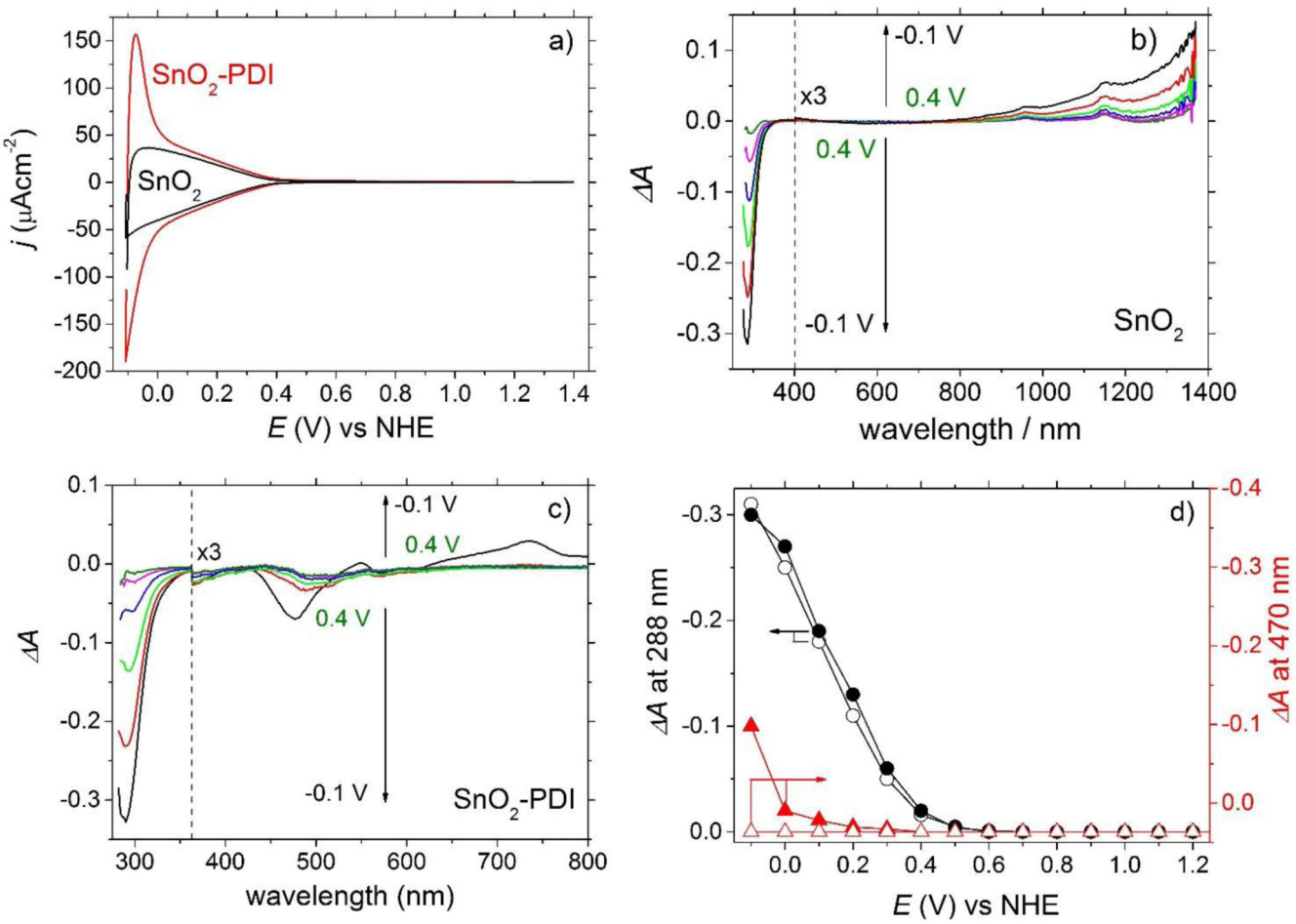

Figure 3.

a) Cyclovoltammetric scans of non-sensitized and PDI-sensitized SnO_2 electrodes in 0.1 M $HClO_4$ aqueous electrolyte (pH 1). b) Potential-dependent difference spectra of non-sensitized SnO_2 electrodes in the same electrolyte. Spectra are recorded after polarization for 1 min at potentials between 1.4 V and -0.1 V (potential steps: 0.1 V). The reference spectrum was measured at 1.4 V. At wavelengths $\lambda > 400$ nm the absorbance was multiplied by a factor of 3 to highlight spectral changes. c) Potential-dependent difference spectra of PDI-sensitized SnO_2 electrodes in the same electrolyte. Spectra are recorded after polarization for 1 min at potentials between 1.2 V and -0.1 V (potential steps: 0.1 V). The reference spectrum was measured at 1.2 V. At wavelengths $\lambda > 400$ nm the absorbance was multiplied by a factor of 3 to highlight spectral changes. d) Potential-dependence of the signal loss (ΔA) at 288 nm (circles) and 470 nm (triangles) observed for non-sensitized (empty symbols) and PDI-sensitized (full symbols) SnO_2 electrodes.

Europe PMC Funders Author Manuscripts

Europe PMC Funders Author Manuscripts

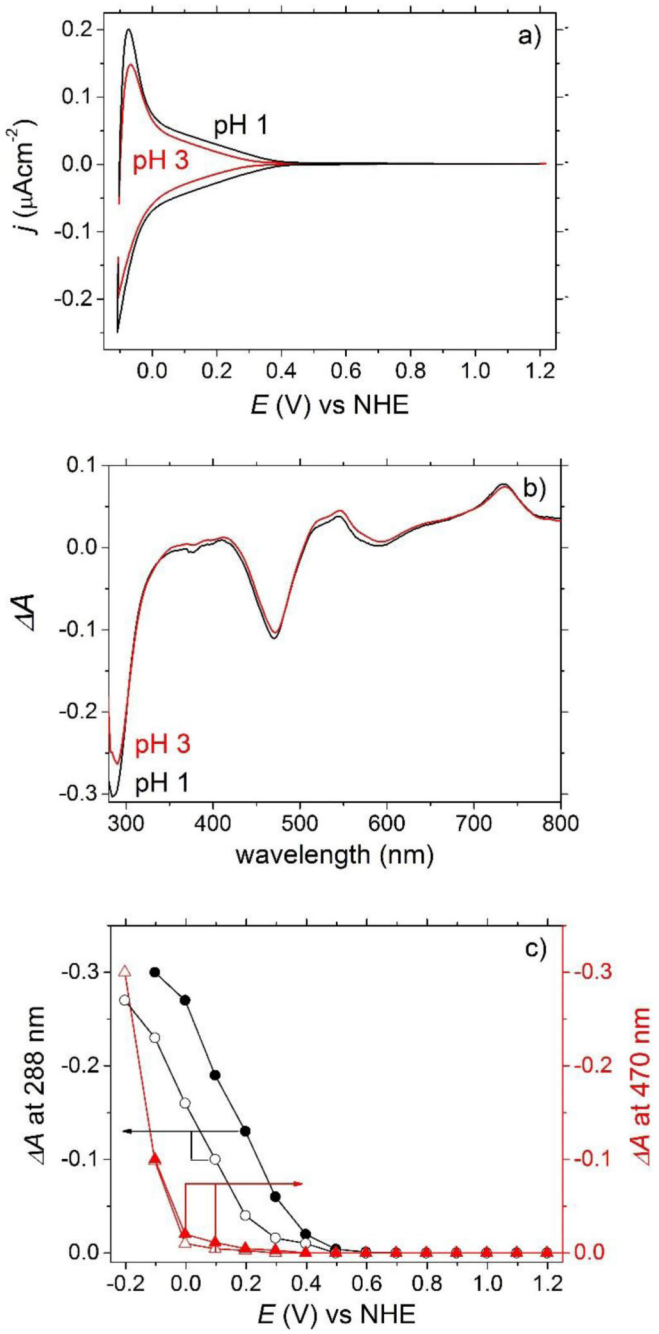

Figure 4.

a) Cyclovoltammetric scans of a SnO_2-PDI electrode in aqueous electrolytes at pH 1 and pH 3, respectively. b) Difference spectra of a SnO_2-PDI film polarized at E = -0.1 V in the same electrolytes. The reference spectrum was measured at 1.2 V. c) Potential-dependence of the signal loss (ΔA) at 288 nm (circles) and 470 nm (triangles) in aqueous electrolytes at pH 1 (full symbols) and pH 3 (empty symbols). Electrolytes: 0.1 M $HClO_4$ (pH 1) and 10^{-3} M $HClO_4$ / 0.1 M $NaClO_4$ (pH 3), respectively.

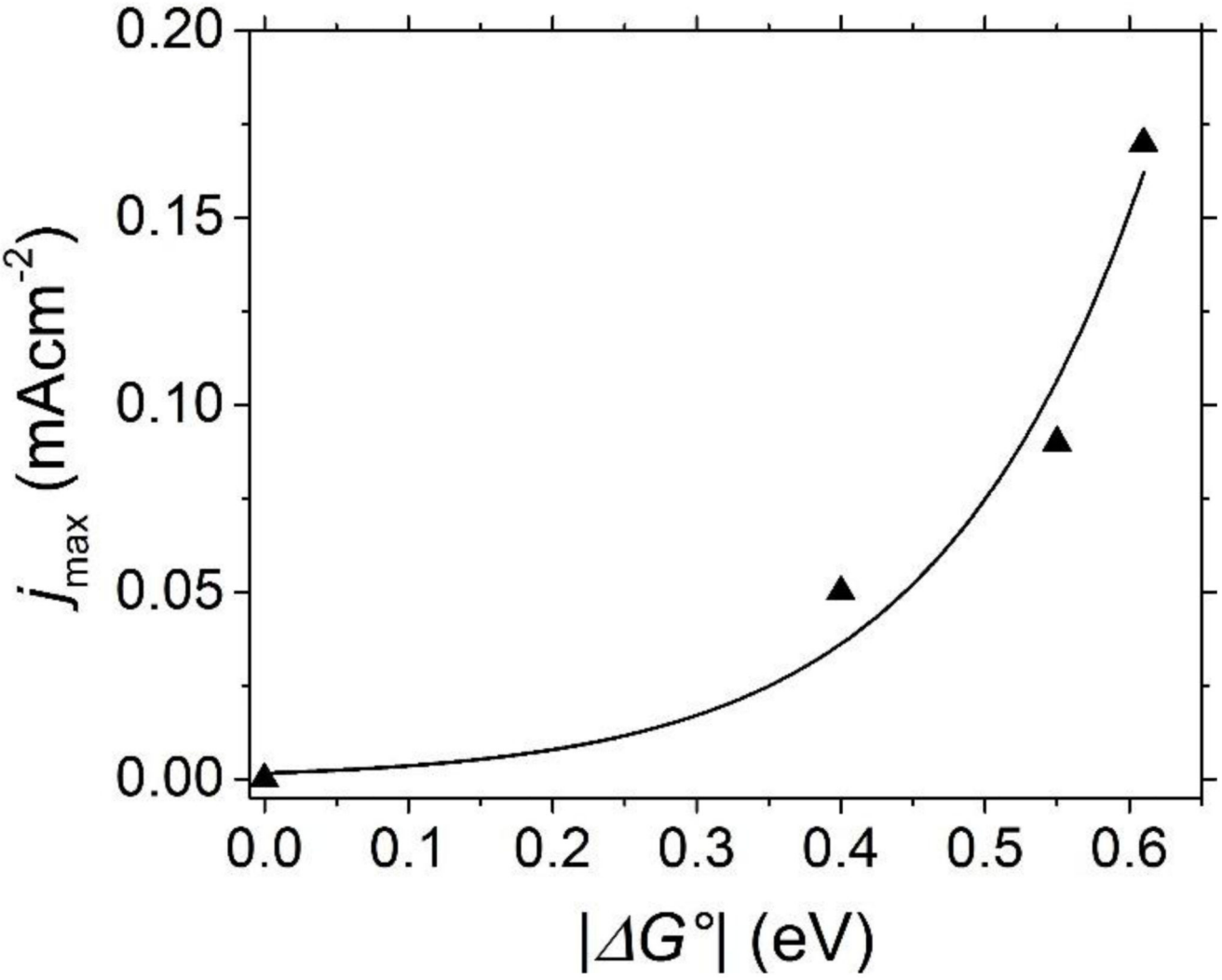

Figure 5.

Limiting photocurrent density recorded for a SnO_2-PDI electrode at 0.8 V as a function of the driving force for electron transfer from PDI* to SnO_2 (ΔG°). The solid line represents the fitting result according to a Gaussian amplitude function.

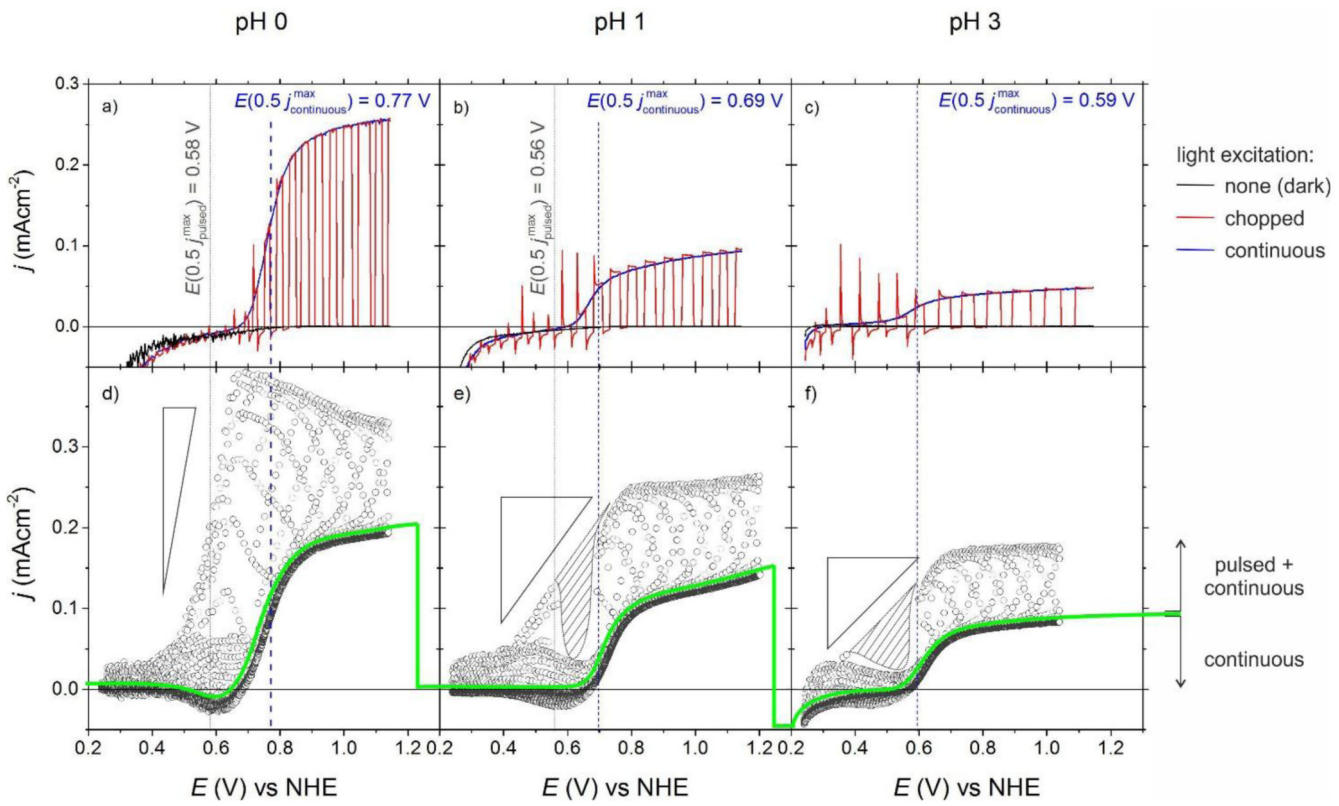

Figure 6.

(a-c) Current-voltage curves of SnO_2-PDI electrodes in aqueous electrolytes at a) pH 0, b) pH 1 and c) pH 3 as recorded in the dark (black line), upon manually chopped (red line) and continuous (blue line) polychromatic illumination. Solar simulator: AM 1.5 G, I = 0.1 Wcm^{-2}. (d-f) Photocurrent transients generated by PDI-sensitized SnO_2 photoanodes in aqueous electrolytes at d) pH 0, e) pH 1 and f) pH 3 upon simultaneous excitation by a pulsed laser (λ = 532 nm, I = 0.06 $mJcm^{-2}$ $pulse^{-1}$) and by a continuous white light bias (AM 1.5 G, I = 0.1 $mWcm^{-2}$). Discontinuous (grey and blue) vertical lines indicate $E(0.5j^{max})$ values i.e. potentials where the photocurrent upon continuous or, alternatively, pulsed light excitation attains ~50 % of its maximum value. The green line in (d-f) separates data points collected during the on-time (pulsed + continuous light) or the off-time (continuous light only) of the duty cycle of the laser. At any time, the electrodes were exposed to the continuous white light bias. Triangles in (d-f) serve as a guide to the eye and indicate the slope of the linear region of transient photocurrents. Electrolytes: 0.1 M NaBr / 1 M $HClO_4$ (pH 0); 0.1 M NaBr / 0.1 M $HClO_4$/ 0.9 M $NaClO_4$ (pH 1) and 0.1 M NaBr / 10^{-3} M $HClO_4$ / 1 M $NaClO_4$ (pH 3). Scan rate: 10 mVs^{-1}.

Europe PMC Funders Author Manuscripts

Europe PMC Funders Author Manuscripts

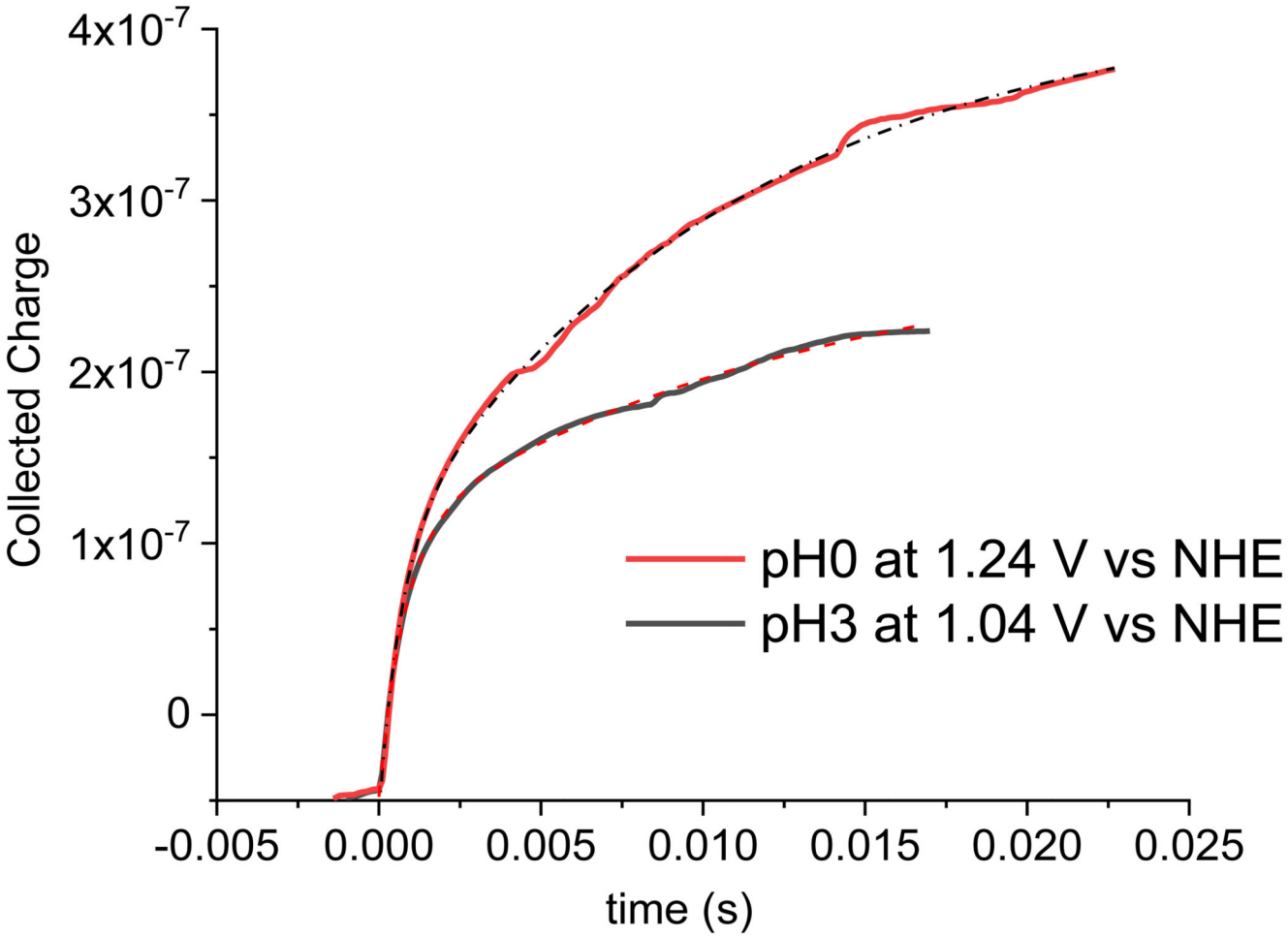

Figure 7.

Transient photocharge generated by SnO_2-PDI following laser excitation in the presence of 0.06 W/cm^2 white light bias. Electrolytes: 0.1 M NaBr / 1 M $HClO_4$ (pH 0) and 0.1 M NaBr / 10^{-3} M $HClO_4$ / 1 M $NaClO_4$ (pH 3). In both cases the applied anodic bias corresponded to the limiting regime of the photocurrent-voltage characteristic.

Europe PMC Funders Author Manuscripts

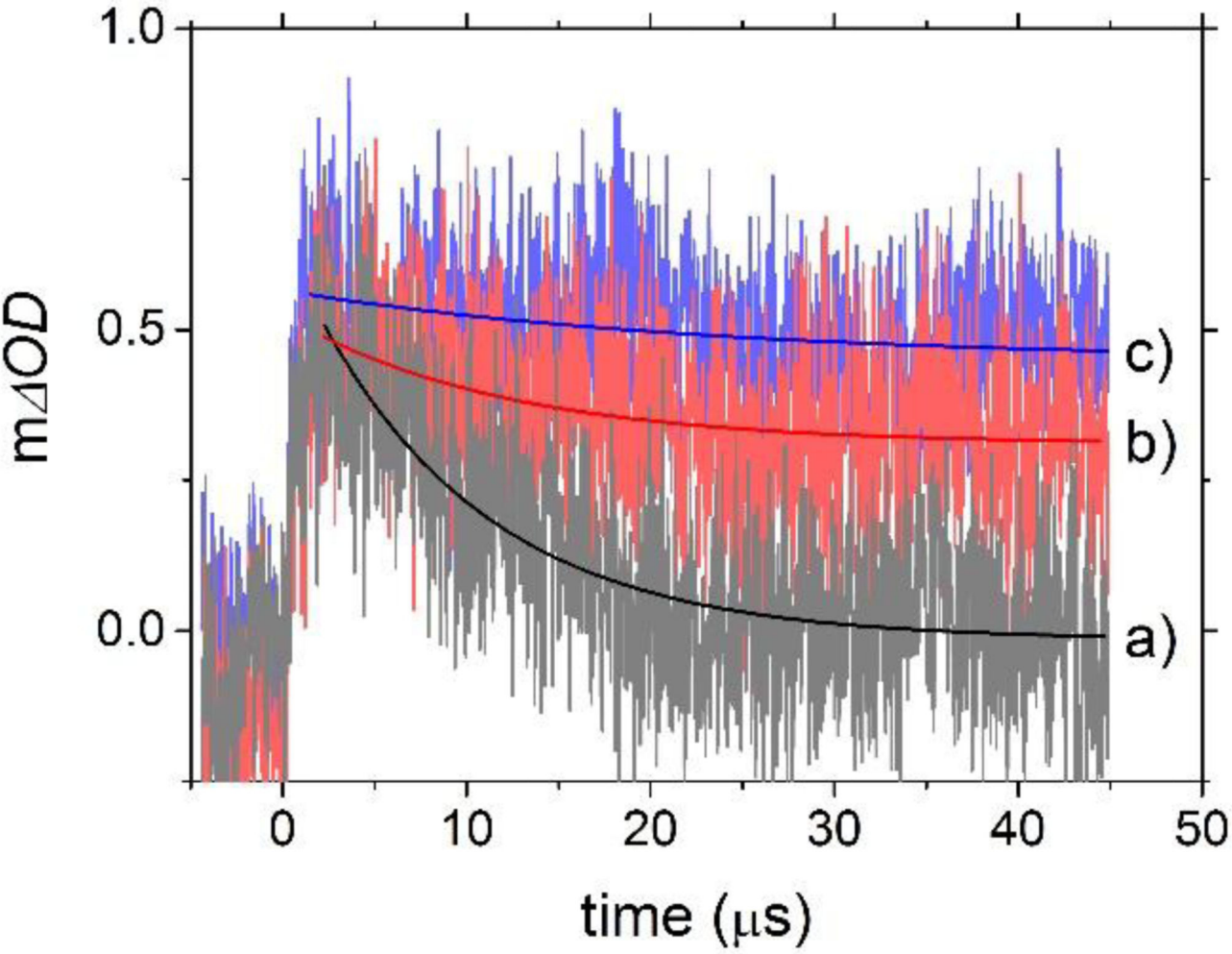

Figure 8.

Kinetic evolution of the absorption feature at 430 nm (due to the $SnO_2(e^-)$-PDI(+) charge separated state) at different anodic applied potentials: E = 1.5 V (blue line), 1 V (grey line) and 0.4 V vs NHE (light blue line), following nanosecond laser excitation at 532 nm; average of 30 laser shots. Electrolyte: 1 M $HClO_4$ (pH 0).

Europe PMC Funders Author Manuscripts

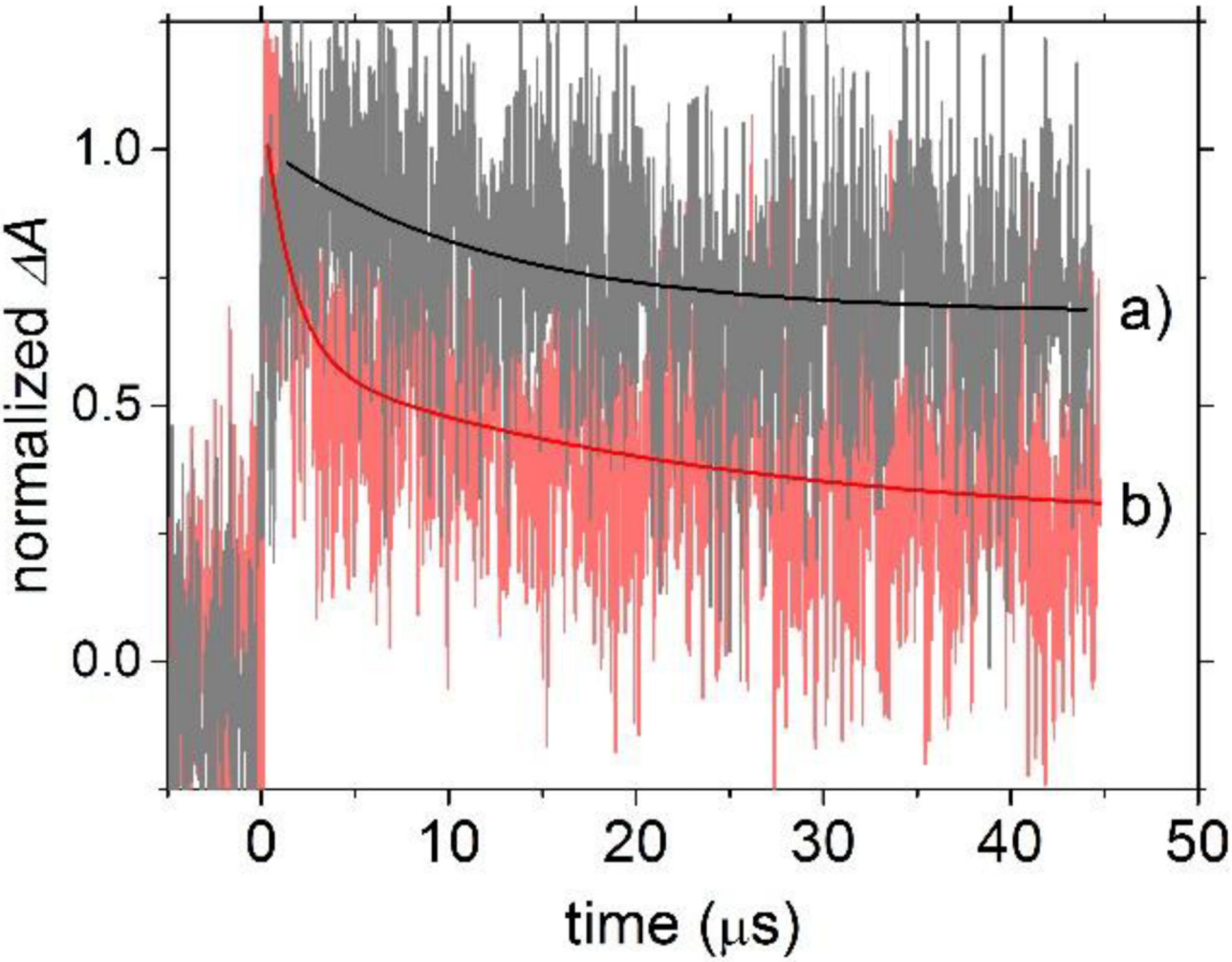

Figure 9.

Kinetic evolution of the normalized absorption difference traces at 430 nm (due to the $SnO_2(e^-)$-PDI(+) charge separated state) in photoanodes polarized at 1 V at pH 0 (grey) and pH 3 (purple). Electrolytes: 10^{-3} M $HClO_4$ / 1 M $NaClO_4$ (pH 3) and 1 M $HClO_4$ (pH 0).

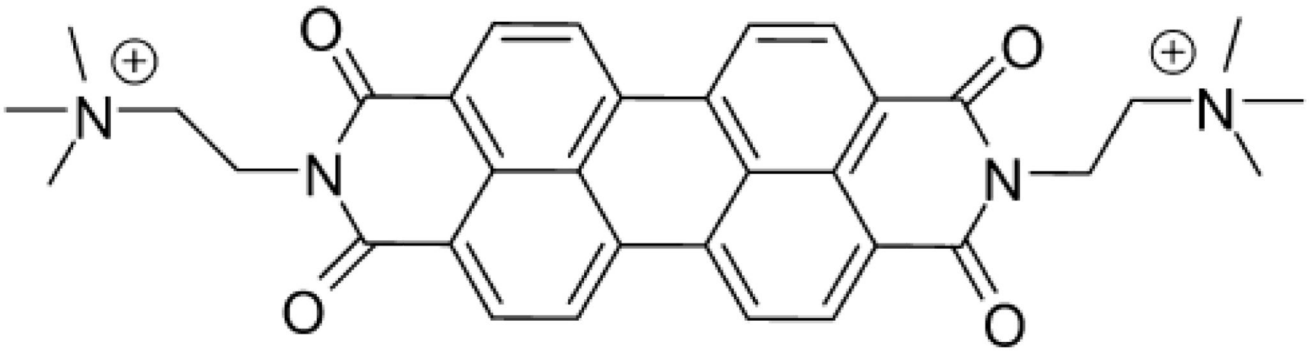

Scheme 1.
Structure of the photosensitizer (PDI).[26]

Europe PMC Funders Author Manuscripts

Europe PMC Funders Author Manuscripts

Table 1

[a]Time constants related to charge separated state recombination at various anodic potentials at pH 0. [b]Ratio between absorbance at t_0 and at a 50 microsecond delay.

	0.4 V	**1 V**	**1.5 V**
Time constant[a]	9.4 μs	14.6 μs	58.4 μs
A_0/A_{50}[b]	5.1	1.5	1.2